Journal of Soils and Sediments (2025) 25:591–608
https://doi.org/10.1007/s11368-024-03828-4

SUITMA12

Soil structure dynamics in constructed Technosols for bioretention cells: X-ray microtomography study

Petra Heckova[1,2] · John Koestel[3,4] · Ales Klement[5] · Radka Kodesova[5] · Michal Snehota[1,2]

Received: 3 March 2024 / Accepted: 23 May 2024 / Published online: 1 June 2024
© The Author(s) 2024

Abstract

Purpose Constructed Technosols are frequently used to create the biofilter layer of blue-green infrastructure elements when the local soil does not possess the necessary properties. However, the long-term functioning of the biofilter is not entirely understood. The aim of this study is to elucidate changes in the structure of a constructed Technosol based biofilter of a bioretention cell (BC) by means of x-ray tomography and additional physical characterization during the first years after installation under two different water regimes.

Methods and materials Two identical experimental BCs were studied to investigate structural changes in biofilter. The BCs exhibited different water regimes. BC1 collected naturally occurring rain concentrated from the nearby roof, while BC2 lacked a regular inflow of water except for several irrigation events and exhibited drier conditions overall. Biofilter was constructed using a mixture of 50% sand, 30% compost, and 20% topsoil. Undistributed soil samples were collected from the biofilter at 7, 12, 18, 23, and 31 months after BC installation. The changes in the soil pore system geometry were assessed by analyzing morphological parameters derived from X-ray computed microtomography images (μCT) and additional physical parameters. The μCT images were analyzed using the SoilJ software package.

Results In both BCs, soil consolidation accompanied by a significant reduction in macroporosity and pore connectivity, occurred between months 7 and 18 in BC1 and between months 7 and 12 in BC2. Macroporosity then gradually increased in BC1 between months 18 and 31. During the same period, in the drier soil of BC2, macroporosity and pore connectivity decreased. In BC1, the water field capacity increased between months 7 and 18, but then returned to its initial values by month 31.

Conclusion The μCT proved to be suitable for assessing the structural changes of constructed Technosol. Significant differences in soil structure development were observed in BC, depending on the water regime. These differences were particularly evident in the development of field capacity, total porosity, and macroporosity.

Keywords X-ray microtomography · Constructed Technosol · Bioretention cell · Soil structure · Infiltration · Swale · Urban soil · Pedogenesis

1 Introduction

Constructed Technosols, which are intentionally created mixtures of organic and mineral waste materials, designed to meet specific criteria, play an important role in runoff formation from the urban catchments (Deeb et al. 2020). Constructed Technosols offer the advantage of precise control over their initial properties and implementation conditions, allowing for tailored compositions to meet specific requirements in various applications (Watteau et al. 2019). Constructed Technosols are significant for blue-green

Responsible editor: Remigio Paradelo Núñez

✉ Petra Heckova
petra.heckova@cvut.cz

[1] Czech Technical University in Prague, Faculty of Civil Engineering, 166 29 Praque, Czech Republic

[2] Czech Technical University in Prague, University Centre for Energy Efficient Buildings, 273 43 Bustehrad, Czech Republic

[3] Agroscope, Standort Reckenholz, Soil Quality and Soil Use, 8046 Zurich, Switzerland

[4] Swedish University of Agricultural Sciences, Department of Soil and Environment, 750 07 Uppsala, Sweden

[5] Czech University of Life Sciences Prague, Faculty of Agrobiology, Food and Natural Resources, 165 00 Prague, Czech Republic

infrastructure, especially in urban areas where natural soils are unsuitable. In summary, constructed Technosols are intentionally designed mixtures of organic and mineral materials that play a crucial role in various applications, particularly in urban environments where natural soils may not be suitable. Their significance extends to the functioning of various blue-green infrastructure systems, including bioretention cells (infiltration swales). Bioretention cells (BC), also known as rain gardens, are soil-plant systems designed to manage stormwater runoff. These depressions in the ground are filled with specialized filter media, called biofilters, and planted with vegetation that is suitable for the local conditions (Davis 2008). Plant species chosen for BCs must be capable of withstanding fluctuating wet and dry conditions, typically falling between those thriving in wetland environments and those requiring drier conditions. Various perennial species, shrubs or trees are best suited to these conditions (Davis 2008; Yuan and Dunnett 2018). These BCs function as natural filters, utilizing processes such as filtration, adsorption, and sedimentation to enhance water quality. Furthermore, they facilitate the mitigation of peak flow and the reduction of the overall runoff volume, thereby conferring hydrologic benefits such as groundwater recharge (Dietz and Clausen 2005; Hatt et al. 2009). Changes in the soil structure of the biofilter affect water infiltration, colloid transport (Mesticou et al. 2016), and heat transport (Malek et al. 2021) in these systems. Compared to natural soils, there is still relatively little literature on the development of soil structure in constructed Technosols (Badin et al. 2009). Séré et al. (2010) found that the pedogenesis processed associated with the development of soil structure, and chemical processes in constructed Technosols are similar to those in natural soils. Additionally, Scalenghe and Ferraris (2009) suggested that the development of soil structure in constructed Technosols is much faster than in natural soils. The hydraulic properties of biofilters and bioretention cells are affected by processes such as consolidation, macropore development, and particle clogging (Coustumer et al. 2009; Muerdter et al. 2018; Zhou et al. 2023). Pedogenesis determines the development of soil structure, changes in organic matter content, formation of macropores, clogging of pores by particles, and alterations of soil wettability. In the case of bioretention cells, the dynamics of structural changes can be influenced by a wetter water regime and growing plants during soil formation (Wang and Zhang 2024). The long-term functioning of BCs is not yet entirely understood due to the scarcity of long-term experimental studies on this topic are still sparse, and the inconsistent results obtained Dietz (2007). The effectiveness of biofilters in bioretention cells for water retention, detention, and purification is dependent on the physical and chemical properties of the soil. These properties are determined by the initial composition of the engineered soil and subsequent soil pedogenesis (Scalenghe and Ferraris 2009; Sere et al. 2012; Jangorzo et al. 2013). Studies have shown that there was no systematic decline in BC performance after two years (Emerson and Traver 2008) and after six years (Jenkins et al. 2010). Coustumer et al. (2009), reported that the hydraulic conductivity of biofilters decreased by more than half from the initial value over seven years. Similarly, Paus et al. (2016) found that the saturated hydraulic conductivity (K_s) of biofilter decreased with decreasing air temperature. Other studies (Archer et al. 2002; Hatt et al. 2009; Muerdter et al. 2018) have demonstrated that vegetation can prevent the clogging of the biofilter, which is a long-term solution for maintaining functioning.

Recently, noninvasive imaging methods such as x-ray computed microtomography (µCT) (Cislerova et al. 1988; Grevers et al. 1989; Schlüter et al. 2020), neutron imaging (Kaestner et al. 2016), and magnetic resonance (Tan et al. 2011; Dohnal et al. 2013) assess soil structure development. X-ray µCT, in particular, is an effective mean of assessing soil structure. These methods enable the determination of soil pore structure with high accuracy while preserving the integrity of the sample, which is a significant advantage (Wang and Zhang 2024). Following µCT imaging, the other important soil properties can be determined by standard destructive methods. X-ray µCT can be used to study soil structure development, pore clogging and pore geometry deformations (Jarvis et al. 2017; Cnudde and Boone 2013; Helliwell et al. 2013). In the investigation of soil structure, µCT imaging has been predominantly applied to agricultural soils. E.g. Koestel and Schlüter (2019) assessed the structural evolution namely the pore morphology and deformations over two years at six time points in an undisturbed soil sample using µCT. After imaging, the samples were returned to the field. Settlement and compaction were observed, primarily below a depth of 20 mm. Coustumer et al. (2009) presented a similar result, demonstrating that small particles settle primarily in the upper 10 cm layer below the surface. Vanderborght et al. (2002) used X-ray µCT to examine the macropore network in loamy forest soil. The study found that a dense macropore network at a depth of 10–20 cm facilitated homogeneous transport, while the presence of isolated large continuous macropores at a depth of 50–60 cm resulted in more heterogeneous transport. Similarly, freshly harrowed soil typically exhibits a macro-structure that resembles an amalgamation of soil aggregates of varying sizes. This is accompanied by a well-connected network of larger pores interspersed among them (Dexter et al. 1983; Schlüter et al. 2018). Some studies have included repeated soil sampling at a specific site over longer time intervals to quantify soil structure evolution using X-ray imaging (Sandin et al. 2017; Keller et al. 2017). In some cases, constructed Technosols structure was examined using µCT. Jelinkova et al. (2016) studied the

state of pedogenesis on undisturbed soil samples by means of microCT. A useful tool for processing µCT images is the SoilJ plugin (Koestel 2018) implemented in the ImageJ (Abramoff et al. 2004). SoilJ has been shown to significantly reduce the time required for processing large image data sets. Although studies on the long-term functioning of bioretention cells are limited and results can vary, non-invasive imaging methods, including µCT have emerged as effective tools for assessing soil structure evolution and its effects on water flow. Further research is needed to enhance the understanding and optimize the design and maintenance of constructed Technosols, particularly in bioretention cells, for long-term performance and behavior.

The main objective of this study is to analyze how the soil structure in the biofilter of a BC evolves. We focus on how the characteristics of the soil's porous space, determined using X-ray µCT imaging, change over time. Additional aim was to assess trends in total porosity and field capacity obtained from standard laboratory measurements as well as characteristics of macropores obtained using µCT.

The additional objective was to assess the differences in biofilter soil evolution in bioretention cell with a water regime typical for the humid temperate climate in contrast to biofilter of the bioretention characterized by drier conditions due to less frequent and restricted water inflow, which instead of that can represent climate with dryer conditions.

2 Materials and methods

2.1 Experimental site and bioretention cells set-up

In December 2017, two identical experimental BCs were established at the University Centre for Energy Efficient Buildings (UCEEB) of the Czech Technical University in Prague (CTU). UCEEB is situated in Bustehrad, Czech Republic (50°9.41797'N, 14°10.19195'E, 355 m a.s.l.). The test site is located in a temperate region with an average annual rainfall of 500–550 mm and an average air temperature of 9 °C. BCs were constructed for long-term monitoring and to evaluate the rainfall-runoff characteristics, assess biofilter property development, and testing of resistant perennials. The set-up is described in detail by Heckova et al. (2022), therefore only basic description is provided here. Each BC is 2.4 m wide and 4.0 m long. The top layer of BCs was made of a 5 cm thick layer of gravel fraction 16/32 representing a mulch layer designed to suppress the weed growth and reduce evaporation. A biofilter was placed under the mulch layer. The biofilter was 30 cm thick at the lowest point and consisted of 50% sand, 30% compost, and 20% topsoil. The texture of the biofilter was: 12% clay (< 0.002 mm), 14% silt (0.002–0.05 mm) and 74% and sand (0.05–2 mm). The drainage layer of the biofilter had an average thickness of 19 cm and was made of gravel fraction 16/32. The drainage pipe collected water from the drainage layer. A layer of sand (0/4 fraction) 10 cm thickness separated the biofilter and the drainage layer to capture fine particles. A geotextile with a grammage of 200 g m^{-2} was inserted under the sand layer. The filling of the biofilter was isolated from the surrounding soil by a waterproofing PVC membrane. A more even distribution of water along the length of the BC was achieved by a shallow gutter made of concrete tiles built at the floor of the BC in the longitudinal direction. The space between tiles was however not sealed, therefore water infiltrated preferentially close to the inlet especially during less intense rain. Each bioretention cell (BC) was planted with four perennial species. The selection of perennials for planting was undertaken with the intention of ensuring sustained growth throughout the experiment. Species capable of withstanding both waterlogged and dry conditions were chosen, with the collaboration of a landscape architect guiding the selection process. The result was the establishment of distinct habitats within the bioretention cell, comprising four specific perennial species. The supplementary material Fig. S1 displays the planting plan of species and their distribution, which included *Aster novae-angliae* 'Purple Dome'; *Hemerocallis* 'Lemon Bells'; *Eupatorium* 'Phantom'; *Molinia caerulea*. In spring 2019, *Eupatorium* 'Phantom' (five pieces of plant) replaced the perennial *Euphorbia amygdaloides* from the original planting plan in 2018 due to unsuitable conditions in the bioretention cell. The study presented in this paper began on 14/12/2017, when bioretention cells were constructed, and finished on 18/06/2020 after the final collection of the soil samples.

2.2 Water and thermal conditions of biofilter

The first BC1 collected stormwater from the roof of the nearby experimental building (roof area 38 m^2, bitumen roof sheets, slope 14°). Input of water into BC1 was therefore the sum of water that falls directly on the surface of the biofilter and water that was collected from the roof. BC2 received rainwater on its surface and was also flooded during ponding experiments. The ponding experiments sought to assess the bioretention cell's performance under controlled conditions with maximum loading in the previous study Heckova et al. (2022). Inflow to the cell matched the area's maximum rainfall intensity with a 5-year recurrence interval. Two types of precipitation were performed: one with high rain intensity and short duration and the other with low rain intensity and long duration. During these experiments, water was supplied from the reservoir, and the inflow system to the BC was identical to that of BC1. A total of six ponding experiments were conducted in 2018 and another six were performed in 2019. Details on the ponding experiments were given by Heckova et al. (2022).

The biofilter's conditions has been continuously monitored since its establishment. There were five soil tensiometers (T8, Meter Environment, Germany) installed at different depths, and four TDR (CS635, Campbell Scientific, U.S.A.) installed at a height of 15 cm above the biofilter-sand interface. The probes labelled as TDR1 through TDR4 were placed in BC1, where TDR1 and TDR4 were located close to the inlet, while TDR2 and TDR3 were farther from the inlet. Similarly, in the BC2 biofilter, TDR5 and TDR8 were located nearer to the inlet, while TDR6 and TDR7 were located farther away from the inlet. Each TDR sensor provided readings of the soil conditions in the root system of specific plants, namely: *Hemerocallis* (TDR4, TDR8), *Aster* (TDR1, TDR5), *Eupatorium* (TDR2, TDR6), and *Molinia* (TDR3, TDR7).

Both biofilters water content conditions were characterized by the weekly minimum and maximum values of the volumetric water content measured in the biofilters during the entire monitored period (Supplementary material Fig. S2). The supplementary materials Fig. S2a and S2c display the biofilter water content closer to the inlet of BC1 and BC2, respectively. The supplementary materials Fig. S2b and S2d display the volumetric water content closer to the outflow of the BC1 and BC2, respectively. The volumetric water content values in bioretention cell BC2 were significantly lower than those in BC1, because BC2 was not connected to a permanent source of rainwater. Lower volumetric water content values in BC2 were observed since September 2019 after the last ponding experiments were conducted. The average volumetric water content of the biofilter in BC1 was 0.3 cm^3 cm^{-3}, while in BC2 it was 0.25 cm^3 cm^{-3}.

Daily minimum, maximum, and mean near-surface soil temperatures measured 18 and 17 cm in BC1 and 18 and 13 cm in BC2, respectively, above the biofilter-sand interface are shown in Fig. 1 along with 15 min of rainfall depth. The temperature data from the temperature sensor built in ceramic cup of tensiometers are only available from April 14, 2018, after the sensors were connected to the data logger. It is evident that the soil at this depth only froze during the winter of 2018/2019. Figure 1 also displays the water input for each BC normalized to a bioretention cell size of 9.6 m^2.

The photographs presented in Fig. 2 illustrate the growth of vegetation during the study period. The photographs were taken from locations with a water supply. In BC1, *Hemerocallis* and *Aster* are in the foreground, while *Molinia* is in the back row on the left and *Euphorbia/Eupatorium* on the right. In BC2, the front row has *Aster* on the left and *Hemerocallis* on the right, and the back row has *Euphorbia/Eupatorium* on the left and *Molinia* on the right.

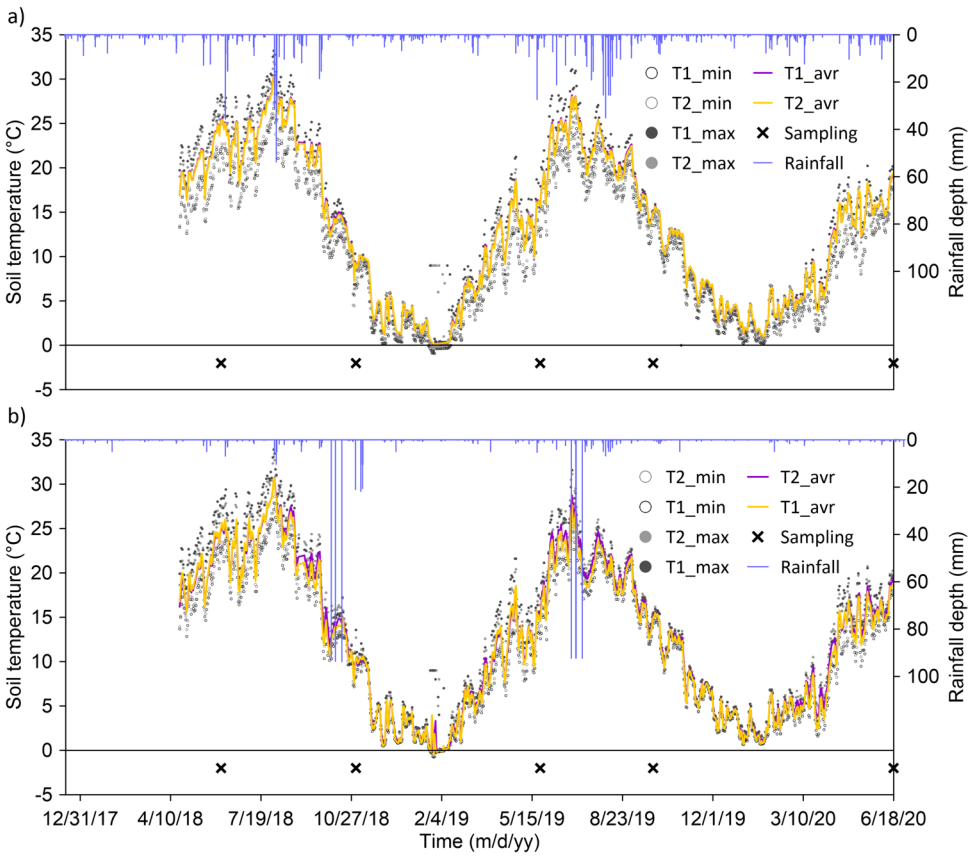

Fig. 1 Biofilter conditions: Biofilter conditions: **a** Soil temperatures measured in BC1 by temperature sensors built into the ceramic cups of the T8 tensiometers at 18 cm (T1) and 13 cm (T2) above the biofilter-sand interface; additionally, the rainfall depths per 15 min are shown (direct rainfall plus roof supply) **b** Soil temperatures measured in BC2 by temperature sensors built into the ceramic cups of the T8 tensiometers at 18 cm (T1) and 13 cm (T2) above the biofilter-sand interface; again, the rainfall depths per 15 min are shown (direct rainfall plus water added during the ponding experiments)

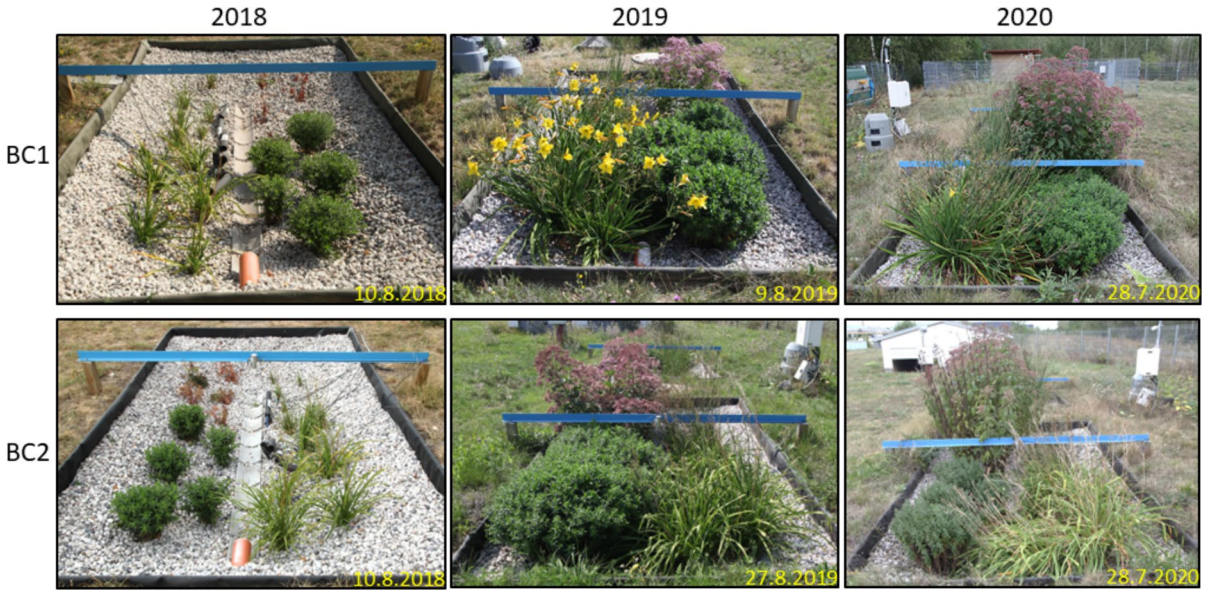

Fig. 2 Photographs showing the vegetation growth during the sampling period in BC1 and BC2

2.3 Collection of soil samples

Intact soil samples were taken from the biofilter layer at five different times over three consecutive years, starting in 2018. Samples were taken from the surface layer of the biofilter at a depth of 0–10 cm. The sampling was done using small aluminum cylinders with an internal diameter of 29 mm and a height of 29 mm (Fig. S3). A detailed description of the sampling schedule is presented in Table 1. After collection, the samples were stored in a refrigerator before further processing. Tables S1 and S2 in the Supplementary material show the sample annotation for each sampling event. Three replicated samples were taken from the vicinity of each plant for each time X-ray µCT of soil samples.

The samples were saturated with water, weighed, and placed in a pressure extractor (Soil Moisture Equipment Corp., Goleta, CA) to equilibrate a field capacity (FC) value (at -330 mbar) before undergoing µCT imaging. After scanning, the samples were dried and reweighed. Porosity, bulk density of the dry sample and water content at a pressure of -330 mbar were calculated from the measured data for all scanned samples. The particle density of the biofilter, set at 2563 kg m^{-3}, was employed to calculate the porosity.

Samples were imaged at two research infrastructures based on availability. Even though the µCT imagers were of different brands at each of the infrastructures, both were state-of-the-art industrial/research grade instruments and imaging conditions were similar in both cases. The samples from 2018 and 2019 were scanned at the Swedish University of Agricultural Sciences, Uppsala in Sweden (SLU), using a GE Phoenix industrial X-ray scanner with a 240 kV X-ray tube with a tungsten target. The samples were imaged using a tube voltage of 100 kV and a current of 200 µA. Each radiograph was exposed for 200 ms. The projections were inverted to 3-D images using the GE software Datos X (version 2.1) and exported as 16-bit TIFF with voxel edge a 20 µm. The samples taken in autumn 2020 were scanned at the Czech University of Life Sciences, Prague on a Nikon XT H 225ST. The tube voltage and current were set to the same values as for imaging at SLU. The 3-D image resulting from 2785 slices with voxel edge length 12 µm was exported. The projections were

Table 1 Detailed description of sampling and µCT imaging

Sampling campaign no.	Sampling campaign name	Sampling date	Number of months after BC foundation	Number of samples taken from each BC	µCT imaging facility	Date of µCT imaging
1	18jun	5.6. 2018	M7	12	SLU	11.11. – 14.11. 2018
2	18nov	1.11. 2018	M12	12		
3	19may	24.5. 2019	M18	12		11.11. – 14.11. 2019
4	19oct	15.10. 2019	M23	12		
5	20jun	18.6. 2020	M31	12	CZU	1.7. 2020

then inverted to 3-D images using the VGSTUDIO MAX 2022.4 and exported as 16-bit TIFF.

2.4 Image processing and analysis

The image data was processed using the FIJI distribution of the open access software ImageJ (Abramoff et al. 2004; Schneider et al. 2012). An example of raw images is presented in Fig. 3a. The samples in Fig. 3 were randomly selected from three replicated samples collected at each sampling point in BC (S1-S4). For image processing, the ImageJ plugin SoilJ (Legland et al. 2016; Koestel 2018) was utilized. Firstly, the µCT images from Jun 2020, which were scanned at higher resolution, were resampled to achieve the same voxel size 20 mm for all the images. This was done in order to facilitate comparison with the previous data set. The raw images were straightened and centered aluminum column outlines were detected automatically. The horizontal slices extending above and below the upper and lower ends of the soil columns were removed from the 3D images. The X-ray images were calibrated to the 0.1 percentile of the grey-values inside the soil volume and the grey value of the aluminum column wall. The two imaged phases were assigned to grey-values of 5,000 and 20,000, respectively. Segmentation of the images was done on the normalized images by global thresholding, where all voxels with value below 8000 were considered as pores. The threshold value was carefully selected based on visual inspection of many normalized images. The same value of threshold was used for segmentation of all µCT images. A single threshold value could be used for the segmentation because the images were normalized in the previous step (Koestel 2018). An example of segmented 3D µCT image is shown in Fig. 3b, with the red color indicating the pore space. The representative cylindrical part (ROI) of the sample was extracted by removing the parts of the sample affected by sample extraction. In the final post-processing step, we removed all isolated outlier pores with a diameter smaller than 80 µm (Koestel et al. 2020), which is the minimum pore size commonly defined as microporosity (Reginato and Bavel 1962). Given the image resolution, it is reasonable to assume that these isolated, thin clusters predominantly represented noise.

2.5 Analysis of pore space morphology

After segmentation, the morphological properties of the brighter phase of a binary image were analyzed. This includes the macroporosity, pore thickness, and three connectivity metrics, the normalized Euler number χn, the connection probability Γ (–), and the critical pore diameter d_c (mm). The characteristics were determined by binary images within the ROI. The ROI represents a cylindrical shape with a diameter of 20.48 mm. Its height is chosen based on the sample to cover its undisturbed portion. The connection probability Γ (Renard and Allard 2013) was calculated using SoilJ, as determined by

$$\Gamma = \frac{\sum_{i=1}^{N} n_i^2}{\left(\sum_{i=1}^{N} n_i\right)^2} \quad (1)$$

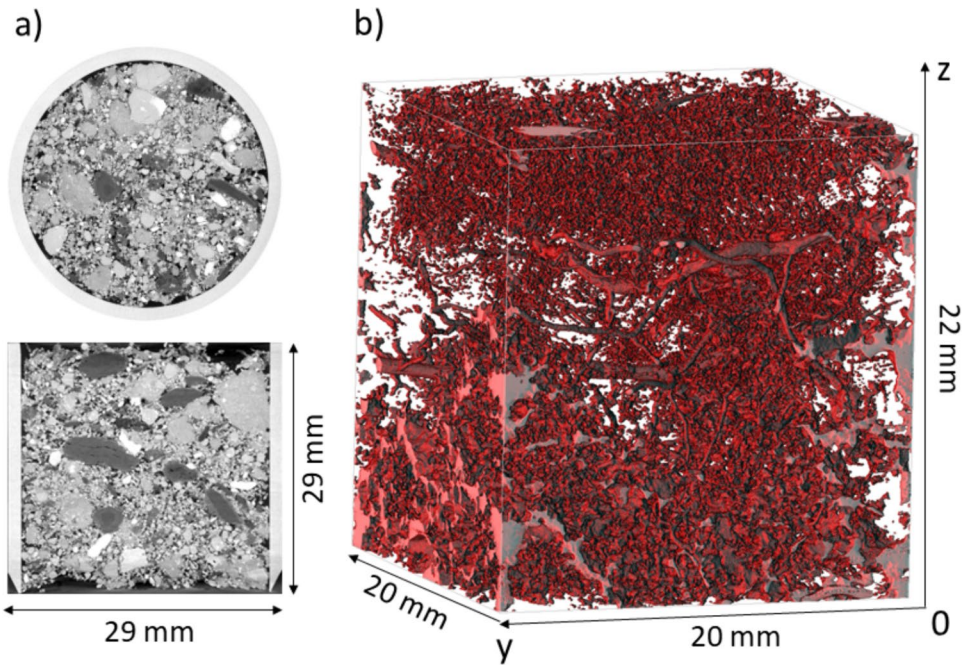

Fig. 3 **a** 2D horizontal (top) and vertical (bottom) cross-section through the raw µCT image **b** 3D µCT segmented image. The red part represents the pore space and the transparent part the soil matrix and solid phases

where n_i represents the number of voxels contained in the ith pore cluster, and N represents the total number of unconnected pore clusters. The macroporosity φ was calculated as the fraction ratio of pore volume in the ROI for each sample. The thickness of the pores was determined using the largest inscribed sphere method, from which the diameter was obtained. The value of Γ equals one when all pore voxels in the investigated ROI are connected. If no pore clusters were present in an ROI, the connection probability of zero was assigned. The closer this value is to one, the higher the connectivity between the pores. Another important parameter in the characterization of porous media is the critical pore diameter d_c. This represents the diameter of the largest sphere that can pass through the pore network within a specific ROI, extending from the top to the bottom. This parameter measures of the narrowest bottleneck pore diameter present in the pore network connection from top to bottom surfaces, which is critical for assessing the permeability of porous media. Three connectivity measures were calculated using MorphoLibJ (Legland et al. 2016) to determine the Euler-Poincaré number χ. Euler's Poincaré characteristic is a metric that quantifies the difference between the number of isolated pore clusters and the sum of loops or redundant connections within these clusters. It provides valuable insights into the connectivity and structure of the porous network. The Euler-Poincaré characteristic (χ) serves as an extensive metric that scales with the volume of the ROI under consideration. To enable comparison across various scales, we normalize χ by the volume of the ROI, resulting in the Euler density (χn) expressed in cm^{-3}. Negative χn values indicate well-connected pore networks, which suggest efficient fluid flow pathways. Conversely, positive values indicate a greater number of isolated pore clusters, which could hinder fluid movement within the porous medium.

2.6 Statistical analyses

The basic statistical parameters, i.e., median, upper, and lower quartile, maximum and minimum were calculated for each sampling event. We conducted an analysis of variance (ANOVA) with $\alpha = 0.05$ significance level to test for significant differences between values obtained from different samplings. Subsequently, the Duncan's multiple range test the significance was performed to assess differences between values obtained from different samplings. The multiple range test was conducted using the XLSTAT Free package in Microsoft Excel (Lumivero 2024). Correlations between soil characteristics obtained using different techniques were assessed using the Pearson product-moment correlation coefficient. The statistical significance of the estimated correlations was evaluated using the p-value. All statistical analyses were performed using significance level of 0.05%. The next ANOVA test was conducted to determine the effect of the water regime on the evolution of soil structure in the biofilter. Porosity and macroporosity were selected as the two characteristics to describe the evolution in the biofilter. The null hypothesis that the water regime does not affect the development of macroporosity and porosity in the biofilter was tested. The hypothesis underwent testing in various periods: throughout the entire study period, during the two-year period when the ponding experiments were conducted, during the six-month period without ponding experiments, the first year of period and second year of period.

2.7 Vegetation maintenance and growth

Following the planting of the bioretention cells, both bioretention cells were watered (40 L per BC) in order to ensure the successful establishment of the plants. During the growing seasons, any unwanted species were removed on a regular basis. In early spring, dry biomass was systematically removed with the intention of allowing the perennials to overwinter and to facilitate better growth (Moller et al. 2011). We photographed the bioretention cells on a regular basis (Fig. 2). The obtained photographs were analyzed in ImageJ software (Abramoff et al. 2004) in order to estimate plant growth metrics. The photographs perspective was adjusted using the Interactive perspective plugin (Schindelin et al. 2012) and the scale of the photographs was adjusted. Subsequently, basic plant metrics (width and height) were quantified based on the aforementioned adjusted photographs. The dimensions are rounded to the nearest ten.

3 Results

As an example of µCT imaging outcomes, Fig. 4 displays a matrix of central slices from selected normalized µCT images. The five columns represent the date of sampling, while the rows indicate the sampling point where the samples were taken, corresponding to the plant in its vicinity, namely S1 = *Molinia*, S2 = *Aster*, S3 = *Hemerocallis* and S4 = *Eupatorium/Euphorbia* in BC1 and BC2. The provided cross sections depict the portion of the sample analyzed by the inscribed circle within the displayed squares. The individual cross-sections were chosen from the center of the sample. As illustrated in Fig. 4, the samples collected from BC2 in months M31 - S2 have an unusually high proportion of organic matter compared to the other samples. These images were excluded from subsequent µCT analysis because the macroporosity value was deemed an outlier. The images demonstrate that samples from site S3 in the BC2 area exhibit higher porosity than other samples from BC2. When compared to BC1, the higher porosity samples are

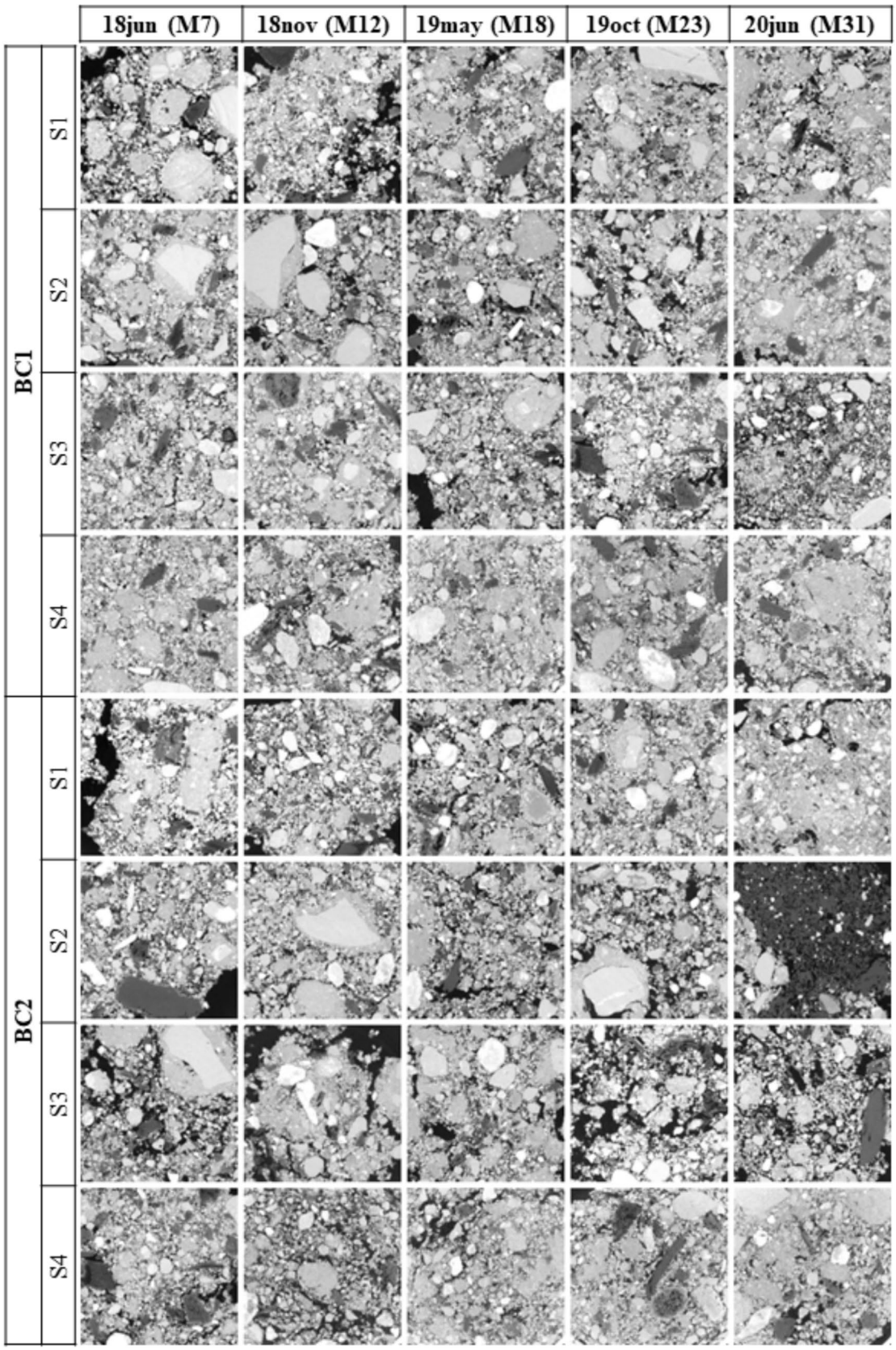
18jun (M7)
18nov (M12)
19may (M18)
19oct (M23)
20jun (M31)
BC1
BC2
S1
S2
S3
S4

◂**Fig. 4** Snippets of vertical 2D cross-section through the µCT images. An example next to each investigated plant species and biofilter was randomly chosen at each sampling occasion. The columns indicate the sampling time, and the rows denote the locations where the samples were taken from (S1 = *Molinia*, S2 = *Aster*, S3 = *Hemerocallis*, S4 = *Euphorbia/Eupatorium*)

observed in the first row of S1, while the most compact samples are seen in the last row of S5.

3.1 Water regime

The total rainfall volume measured by the weather station during the 31 months was 841 mm. The total normalized water input for BC1 during the study period, including direct precipitation and roof water, was 4347 mm. For BC2, the total normalized water input was 1779 mm, which includes rainfall that fell directly on the BC and water added during ponding experiments.

3.2 Plants growth

There was a significant increase in vegetation mass over three years, as shown in Fig. 2. The first photograph taken in 2018 highlights the dead state of the *Euphorbia amygdaloids* plant, while the following image taken in 2019 displays the thriving growth of *Eupatorium* 'Phantom', which has proven to be a highly compatible and flourishing species within the bioretention cell. In 2018 at end of the growing season, the plants in both BCs had achieved similar growth and the average width of the plants in BC1 and BC2 was as follows: *Aster*, 60 cm (height 40 cm), *Hemerocallis*, 30 cm (height 40 cm), and *Molinia*, 10 cm (height 30 cm). Following the conclusion of the 2018 growing season, the *Euphorbia* have withered and was therefore removed. Following the 2019 growing season, the average width of the *Molinia* plant in BC1 was determined to be 20 cm (height 100 cm). The dimensions of the other plants in BC1 were as follows: 120 × 120 cm (height 70 cm) for the *Aster*, 70 × 160 cm (height 60 cm) for the *Hemerocallis*, and 100 × 126 cm (height 90 cm) for the *Eupatorium*. In BC2, the width of the *Molinia* plant in 2019 was 20 cm (height 100 cm). The other plants reached the following dimensions: *Aster* (100 × 170 cm, height 70 cm), *Hemerocallis* (70 × 130 cm, height 60 cm), and *Eupatorium* (100 × 150 cm, height 90 cm). The plant size in 2020 was determined on the date of the last sampling on 6 June 2020 at BC1: the average width of *Aster* was 50 cm (height 30 cm) and *Molinia* 40 cm (height 130 cm). For the other plants, the width and length were: *Hemerocallis* was 103 × 170 cm (height 80 cm) and *Eupatorium* was 120 × 180 cm (height 200 cm). In BC2, the average width of *Aster* and *Molinia* plants was 40 cm (height 30 cm) and 20 cm (height 60 cm) respectively, and the width and length of all plants were: *Hemerocallis* was 100 × 140 cm (height 60 cm) and *Eupatorium* was 90 × 150 cm (height 70 cm).

3.3 Soil properties determined from undisturbed samples

Figure 5 illustrates the development of soil properties (total porosity, bulk density, and FC), and its variability measured on the samples taken from both BCs. The colored symbols represent the corresponding values for the soil samples, with each color indicating the specific plant sampled. Porosity trends in both BCs, whose values ranged from 0.3 to 0.6 are shown in Fig. 5a. In the BCs, porosity decreased significantly after the growing season during the first year of operation between M7 and M12. There was also a very slight decrease in porosity of the BC1 samples in the second and third years, but it was not significant. The median values also decreased in the M12 sampling and reached similar values in M18 samplings. The range of values was lower in samplings before the vegetation season M7 to M18 than after the vegetation season M12 and M23 and during the vegetation season M31. The trend in the porosity values in BC2 after the first year of operation differed from that in BC1. Compared to BC1, porosity increased significantly between the M12 and M18 in BC2. The FC in BC1 (Fig. 5b) showed a gradual increase until M18, and the significant increase in value occurred between M12 and M18. Subsequently, there was a significant decrease in values between M18 and M31. However, the comparison of FC in the last M31 and first M7 sampling showed almost identical values to those obtained in the sample collected shortly after the start. The median values in BC2 remained relatively constant during the first two years, with a significant decrease occurring only in the last year. The maximum and minimum values ranged from 0.12 to 0.35 $cm^3\ cm^{-3}$. During the sampling campaign M12, there was a higher scatter of values. Figure 5c shows the bulk density of the samples, which ranged from 1.1 to 1.6 $g\ m^{-3}$. These values fall within the typical range for sandy soils. As shown in Fig. 5c and a, bulk density was inversely proportional to porosity.

3.4 Macroporosity, connection probability, normalized Euler number

Figure 6a illustrates a decrease in BC1 macroporosity values during sampling campaigns M7, M12, and M18, where the most significant decrease was recorded between months M7 and M18 (according to Fig. 6a). In the M23 and M31 sampling campaigns, no significant change in trend was observed. The values have stabilized and remained almost constant. The macroporosity values in BC1 oscillated between 0.02 and 0.14, while in BC2 they

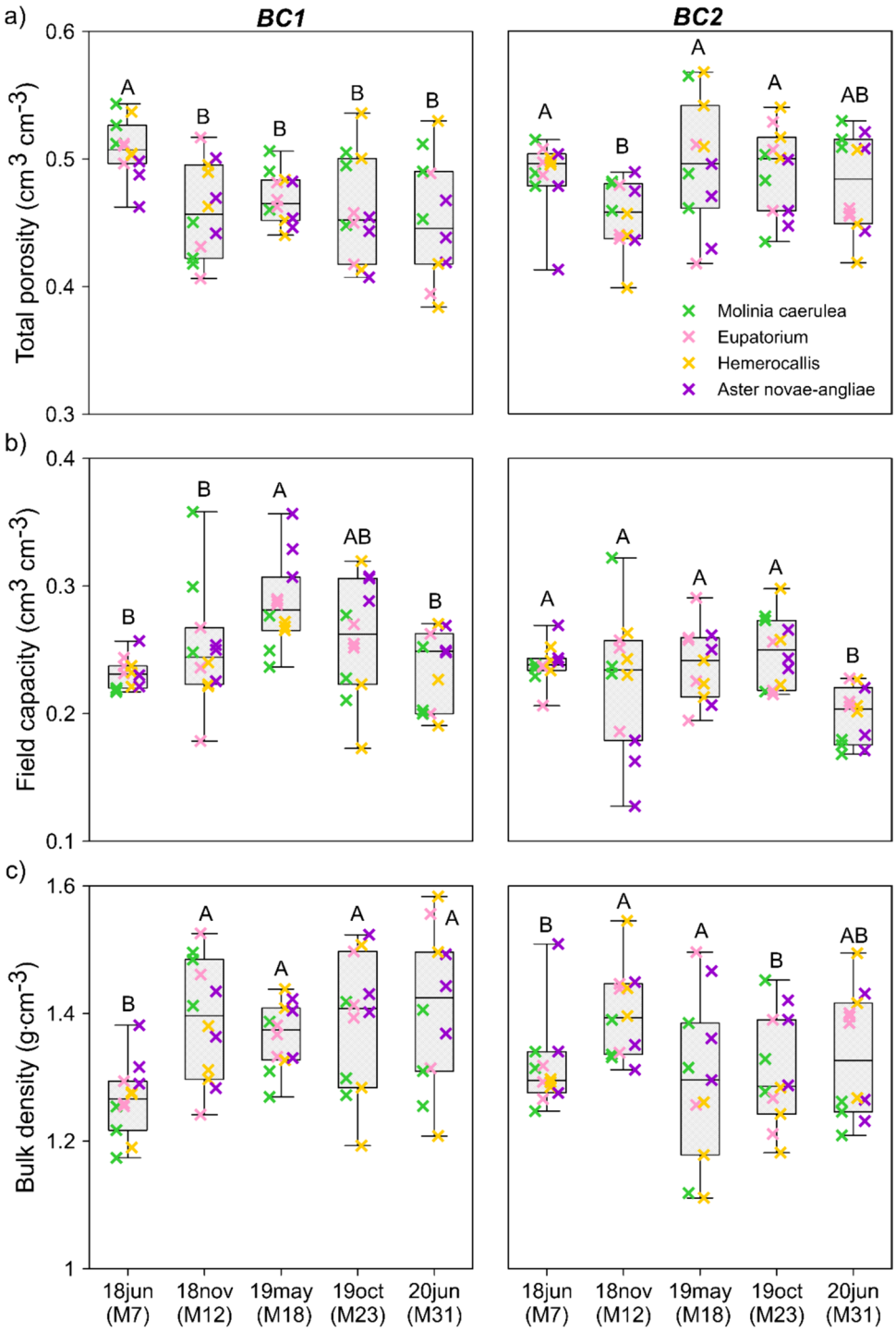

Fig. 5 Biofilter characteristics: **a** total porosity **b** field capacity and **c** bulk density measured on the samples taken from BC1 (left) and BC2 (right) at the 5 sampling campaigns. The upper and lower edges of the boxplot bodies correspond the upper and lower quartile of the observed values, the extreme values to the respective maximum and minimum values. The line marks the median value. The letter labels in the box plots indicate the level of significance ($p < 0.05$) for each characteristic between individual batches of samples

ranged from 0.02 to 0.18. For BC2, there was a decrease in values from M7 to M12, similar to BC1, but the decrease was less significant. Macroporosity trends (Fig. 6a) were similar to total porosity trends (Fig. 5a) in both cases BCs. Figure 6b shows the connection probability, which reflects the degree of pore connection in the sample. The values in the individual boxes show a wide range for both BCs. For BC1, the values for months M18, M22, and M31 cover the entire range from 0 to 1. A significant decrease in mean values was observed between M7 and M18 and then between M18 and M31. As for the mean value, it increased in M12, then increased again in M31 and stabilized at this level. The connection probability values in BC2 were also highly variable, similar to those in BC1, ranging from 0 to 1 and covering almost the entire possible range. There was a significant decrease between M7 and M12, similar

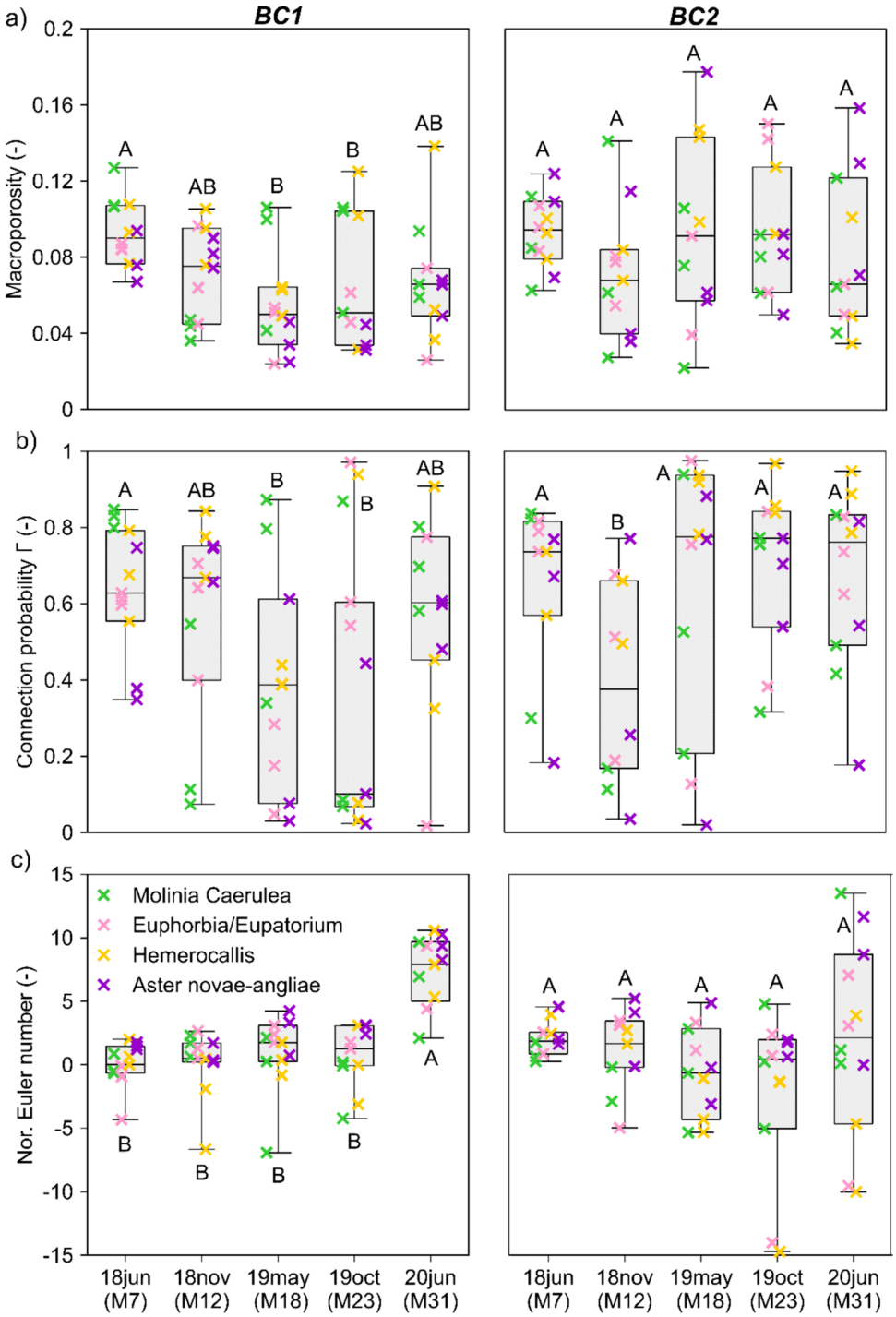

Fig. 6 Biofilter characteristics derived from µCT images: **a** macroporosity **b** connection probability Γ and **c** normalized Euler's number determined from binary images of samples taken from BC1 (on the left) and BC2 (on the right) at the 5 sampling campaigns. The upper and lower edges of the boxplot bodies represent the upper and lower quartiles of the observed values, while the extreme values indicate the maximum and minimum values. The line indicates the median value. The letter labels in the box plots indicate the level of significance ($p < 0.05$) for each characteristic between individual batches of samples

to BC1, and afterwards the values stabilized at a level similar to the initial M7 sampling. The nor. Euler number in Fig. 6c provides information about pore connectivity. For BC1, positive values of the normalized Euler number predominate and occur in a similar range for the first four sampling campaigns. In the last M31, the mean values increase significantly, and only positive values occur in BC1, and positive values predominate in BC2.

3.5 Critical pore diameter, specific surface area and pore thickness

Figure 7a illustrates the evolution of the critical pore diameter. For BC1 (Fig. 7a), the values remained relatively constant throughout the study period with minimal variance. There was no significant difference found between the samplings. In BC2, a significant increase in values was observed

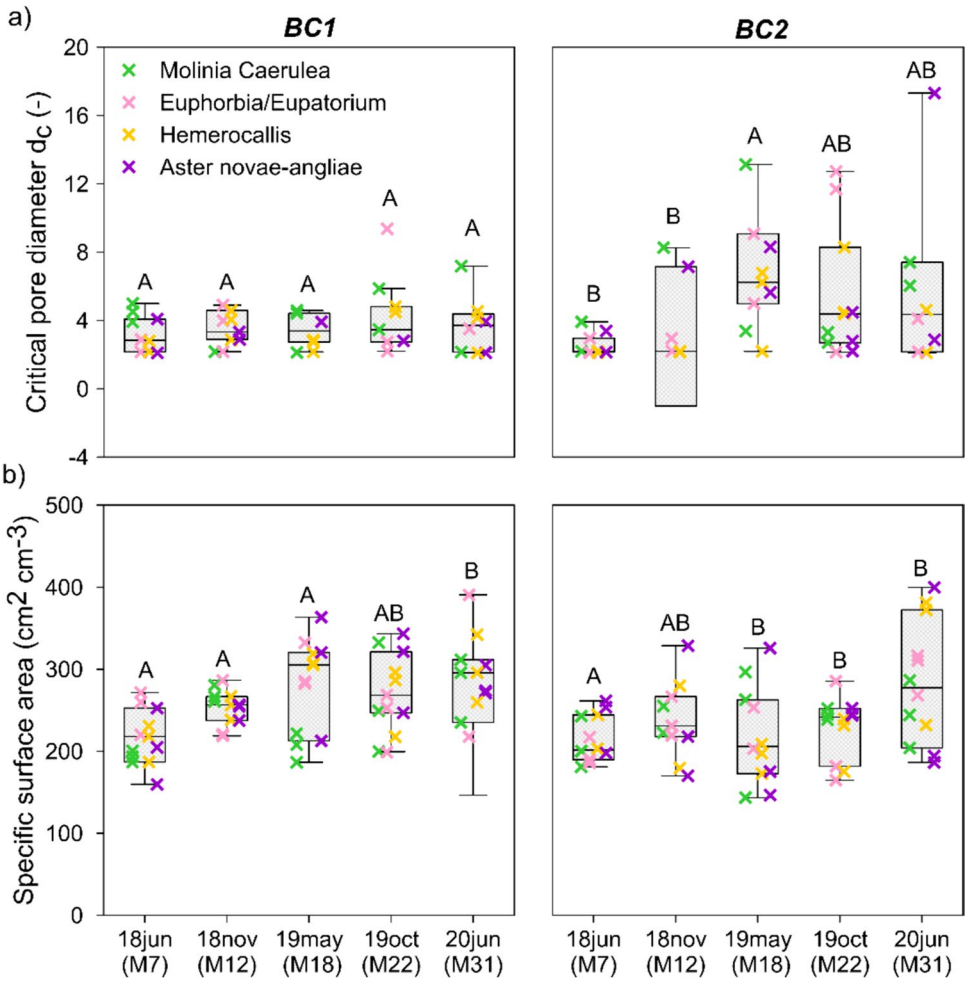

Fig. 7 Biofilter characteristics derived from µCT images: **a** Critical pore diameter and **b** specific macropore surface area determined from binary images of samples taken from BC1 (on the left) and BC2 (on the right) at the 5 sampling campaigns. The upper and lower edges of the boxplot bodies represent the upper and lower quartiles of the observed values, while the extreme values indicate the maximum and minimum values. The line indicates the median value. The letter labels in the box plots indicate the level of significance ($p < 0.05$) for each characteristic between individual batches of samples

between M7 and M18, while in the other samples the values did not differ significantly from the previous ones. Compared to BC1, BC2 showed a significantly wider range of values, except for the first measurement at M7, where the values are comparable to BC1. Figure 7b illustrates the evolution of the specific surface area. A slight upward trend is discernible in BC1, with a pronounced increase between the initial value of M7 and the final value of M31. BC2 exhibits a comparable significant increase, both between the first and last value and between M7 and M18.

For the pore thickness analysis, five categories were created to which pores were assigned a range of values (80–310; 310–540; 540–770; 770–1000; > 1000 µm). The percentage representation of thickness sizes was determined for each sampling. The majority of pores in both BC1 and BC2 fall within the 80–310 µm range, with a lower percentage of pores larger than 310 µm. In M31, there were no pores larger than 1000 µm in bioretention cell BC1 and no pores larger than 770 µm in bioretention cell BC2. The first four samplings for both BCs include pores in all size categories.

Figure 8 displays the correlation matrix for the eight biofilter characteristics quantified in this study. Positive significant correlations were found between the connection probability and macroporosity according to percolation theory (Messing and Jarvis 1990). Also between porosity and bulk density for both bioretention cells BC1 and BC2. Additionally, a negative and statistically significant correlation was observed between specific surface area and connection probability in both BCs. Furthermore, a significant correlation was observed between macroporosity and critical pore diameter, with greater significance noted for BC1. Insignificant correlations were also found at position BC1, including those between FC and nor. Euler number or between the connection probability and the critical diameter. However, significant correlations were found between field water capacity, bulk density and porosity in the case of BC2, with values almost equal to one. Additionally, BC2 exhibited a more significant correlation between macroporosity and nor. Euler number compared to BC1. BC2 contained a greater number of insignificant correlation values, as compared to BC1.

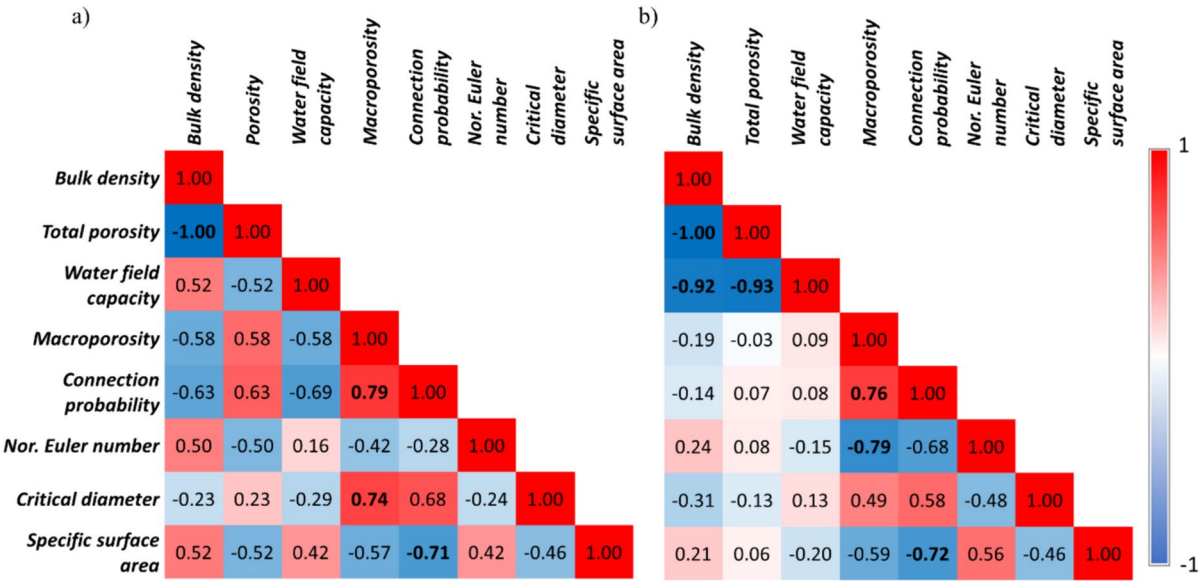

Fig. 8 Pearson correlation coefficients **a** BC1 and **b** BC2 between characteristics of the pore system determined by µCT image analysis and characteristics determined by measurement. Significant correlations are shown in bold font

3.6 Evaluation of the statistical analysis

The study found that both macroporosity and porosity were influenced by the water regime during the entire period under examination. The null hypothesis was rejected with statistical significance observed for both porosity ($p = 0.009$) and macroporosity ($p = 0.027$). However, when only examining values from the first year of operation (M7 and M12), the water regime did not show a similar influence, confirming the null hypothesis. The null hypothesis was also supported in the third year (M31), where only one sampling was conducted and no emergence experiments were performed. A significant effect of the water regime was observed when evaluating the second year of development (M18 and M23), where both macroporosity and porosity were affected with p-values of 0.023 and 0.00093, respectively. Furthermore, the period when ponding experiments took place, i.e. the first two years (M7, M12, M18 and M23), was tested. In this period, null hypothesis was rejected with statistical significance observed for both porosity ($p = 0.033$) and macroporosity ($p = 0.011$). A multiple range test was conducted to compare the characteristics. Significance groups are indicated by the letters next to each boxplot in Figs. 5, 6, and 7. Most characteristics exhibited statistically significant differences among the various sampling. Only macroporosity and normalized Euler's numbers in BC2 did not show any statistical significance, indicating that all samples were characterized at the same level of significance.

4 Discussion

4.1 Uncertainty of image analysis

The µCT imaging was conducted using two instruments under the same x-ray beam parameters, but different image resolutions. To minimize the influence of different pixel sizes on the segmentation the images were resampled to the same resolution prior to further processing. Therefore, we do not expect significant influences of different imaging conditions on experimental results. The segmentation of soil images obtained through µCT carries a degree of uncertainty due to the diversity of soil components, including solid matter, organic material, and air pores (Rippner et al. 2022). The main challenge is to differentiate between organic matter and air spaces, as organic matter includes these pores. Additionally, defining clear boundaries between each component is difficult, making the segmentation process complex (Baveye et al. 2010). The segmentation of soil images obtained through µCT is a complex task, especially when plant roots are present (as shown in Fig. 9a). Plant roots, highlighted in blue in Fig. 9b, can be mistaken for pores due to the presence of air cavities in their internal structure, which can vary depending on growth stage, plant species, and soil conditions. The Soto Gómez et al. (2018) concluded that organic residues frequently serve as transport channels in the soil. In their current state, they exert a significant influence on the hydrological properties of soils and colloid transport.

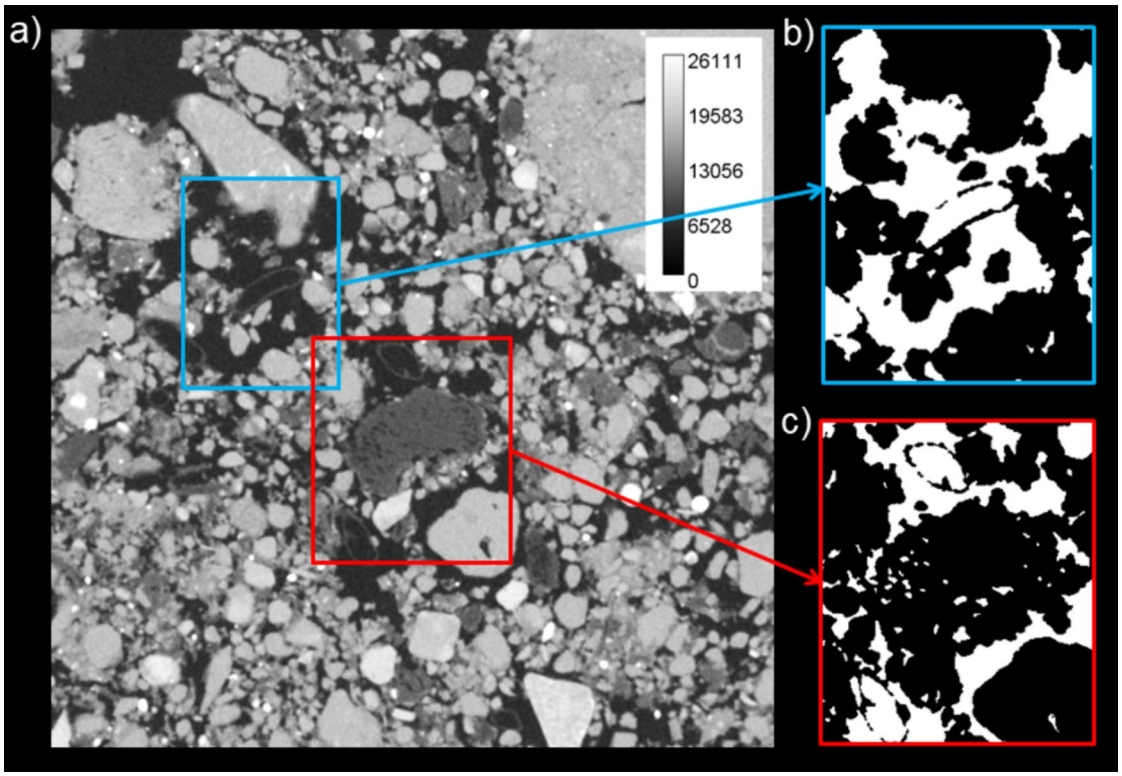

Fig. 9 **a** µCT image with marked segmented parts, focusing on the area containing **b** a root and **c** organic material. The inlay shows the calibrated 16-bit X-ray gray-scale (5000 corresponds to the density of air, 20000 to the density of aluminium)

4.2 Soil characteristics

Consolidation of the biofilter soil resulted in a reduction of total porosity and macroporosity during the first year of operation. This consolidation occurred in both bioretention cells. The limited plant development during the first year did not contribute to an increase in macroporosity due to root growth. The subsequent development of macroporosity likely depended on the growth of the root system and physical processes in the soil (Bodner et al. 2014). For BC1, the largest increase in plant growth occurred during the second year, particularly at M18 and M23. This may have resulted in a greater variation of values during these last two sampling periods, as the root system was already relatively well developed (although not directly measured, it was assumed from above ground plant appearance). For BC2, the largest increase in vegetation was observed during the M12, which also had a higher variation of macroporosity values. The FC values in both BCs were similar in the first sampling before vegetation was planted and were within a narrow range. These samples were taken in M7, before planting any plants. Therefore, it can be assumed that the soil initially had a similar ability to retain water in both cases and was not affected in any way. The bulk density shows values are typical for sandy loam soils, as reported by Schaap et al. (2001). As expected, macroporosity values were lower than total porosity values. The analysis of macroporosity was limited to the central part of the sample with a diameter of 20,48 mm, excluding the smallest pores. In contrast, the evaluation of total porosity included the entire cylinder volume, accounting for partially disturbed soil close to the cylinder walls. Macroporosity ranges from 0.02 to 0.18 for both BCs, which is similar to the values reported for natural soils by Aydemir et al. (2004) and Pagliai et al. (2004). In the case of BC2, the trends in macroporosity are correlated with the trends of total porosity. However, in BC1, a slightly increasing trend in macroporosity is observed from M18 onwards. In both bioretention cells (BCs), there was a positive correlation between the probability of pore connection and macroporosity. This relationship aligns with percolation theory, as illustrated by Jarvis et al. (2017), where visible porosity demonstrates a positive correlation with connectivity also in undisturbed soil. The course of the pore connection probability shows a positive correlation with macroporosity in both bioretention cells (BCs). This relationship suggests that higher macroporosity in the soil leads to a higher connection probability. However, there is a significant scatter of pore connection probability values is also observed throughout sampling period. This variation may be due to various factors, including the diverse development of plant root

systems. Each plant can have a different root system, which affects the soil's ability to pass water. The location of the plants in the bioretention cell overhang may also play a role. Pores located closer to the inlet may be more susceptible to clogging by small particles from rainwater and roof cover, which can affect soil permeability and the likelihood of pore connection probability (Liu et al. 2022).

According to the study by Deeb et al. (2016), the constructed Technosol in the biofilter is suitable for effective water retention in the bioretention systems. The biofilter contains an optimal amount of mineral waste compost (20–40%) that retains water effectively and exhibits properties similar to natural soil. To verify the validity of this claim, a comparison was made with Pagliai et al. (2004) where the macroporosity values of natural soil were similar to in bioretention cells. The water retention properties of the biofilter are confirmed by analyzing the pattern of maximum and minimum volumetric water contents, as shown in Fig. S2. The range from 0.2 to 0.4 cm^3 cm^{-3}, with the biofilter maintaining a constant optimum volumetric water content. Figure 2 demonstrates this capability, showing ideal conditions for plant growth are evident. Zanin et al. (2018) achieved similar results in their study using a very similar soil mix of constructed Technosol in a bioretention cell, with measured volumetric water content values in the same range. Figure S2 illustrates that different plant species produce distinct volumetric water content conditions (Gerke and Kuchenbuch 2007). Because water distribution along the bioretention cell length is enhanced by the concrete gutter the relatively even distribution of inflow water is assumed with possibly slightly more infiltration close to inlet due to leaks between the gutter tiles. From the volumetric water content distribution in Fig. S2, it however can be observed that the driest conditions in BC1 are created by the plant *Hemerocallis* I, despite its proximity to the inflow. A comparison of the volumetric water content of the remaining three plants reveals that they exhibit very similar values. Upon examination of the FC values of the individual plants marked with crosses in Fig. 5b, it becomes evident that these values form fairly regular clusters, corresponding to the different conditions created by the different plant species. This fact is also observed in BC2. A study by Zhou et al. (2020) suggests that plant root systems influence soil macroporosity. Figure 6a illustrates that the samples collected from the *Aster* plant in BC1 form relatively distinct clusters, which is consistent with both macroporosity and total porosity. In contrast, a considerable degree of variability is observed for the *Hemerocallis* plant. This variability may be attributed to various factors, including the sampling procedure and the activity of the organisms (Chen 2018). For instance, the study suggests that the presence of a single larger pore may result in an increase in macroporosity throughout the sample. This prompts the question of whether these values should be considered outliers. The objective of this sampling was to assess the evolution of soil characteristics for the entire bioretention cell, and thus all values were retained for analysis. The study Heckova et al. (2022) conducted by demonstrates that the biofilter effectively serves the purpose of water retention and peak flow reduction. The soil's pore size distribution indicates favorable conditions for plant growth and excellent structure for water retention.

4.3 Soil structure changes

A higher number of isolated pores may lead to a decrease in saturated hydraulic conductivity, which could also affect the hydraulic performance of the bioretention cell. The normalized Euler number in BC1 indicates an increase in the number of isolated pores, which in turn may reduce saturated hydraulic conductivity. This corresponds to a decrease in macroporosity in BC1. On the other hand, the FC in BC1 increased in M18, and FC values returned to their initial values in M31. In relation to BC2, a reduction in the number of isolated pores and burrows was observed. The Euler number indicates positive values, which suggests a decrease in the likelihood of pore connectivity.

The initial sampling in M7 suggests that the pores in BC1 were relatively well connected. The Euler number was represented by both positive and negative values. In the subsequent year, the Euler number values shifted into positive values, indicating less interconnected pores. This finding was supported by a study conducted by Heckova et al. (2022), which reported a decrease in saturated hydraulic conductivity in the same biofilter during the first year after the vegetation season. In the following year, the probability of pore connection decreased while the number of isolated pores increased. Therefore, it can be assumed that the saturated hydraulic conductivity will also decrease in the following periods (Schaap et al. 2001). In M31, there was an increase in pore connection probability. However, the Euler number, which predicted a higher number of isolated pores, also increased, contradicting the previous statement. The macroporosity remained comparable to that of the preceding year, 2019. The analysis of pore thickness showed that the highest concentration of small pores was found in the last sampling M31, which may have contributed to the elevated Euler number. This can be attributed to the substantial presence of so-called transmissive pores, a term established by Pagliai et al. (2004) to describe pores ranging in size from 50 to 500 µm. The significant representation of these pores in the biofilter was evident in Fig. 8. The positive attributes of the biofilter were further supported by (Heckova et al. 2022), who observed a significant peak flow reduction in BC1.

The limitation of the current study is that it cannot distinguish between different causes of observed phenomena. For example, the effect of pores clogging by particulate matter from atmospheric deposition was not studied.

4.4 Impact of conditions in biofilter on soil structure

Soil water content is a crucial factor in soil structure development. Zhang et al. (2019) study shows that drought can significantly reduce hydraulic conductivity and porosity and increase bulk density in the upper 0 to 10 cm of soil. In this study, BC2 had lower overall water contents and irregular water inflow compared to BC1. In 2018 and 2019, infiltration experiments were conducted to fully saturate the biofilter with water. Starting in 2020, the water content of the biofilter in BC2 began to decrease, potentially causing drought stress in the plants. The macroporosity graph indicates a clear decrease in the first year, which is attributed to soil consolidation. However, there is a further decrease in macroporosity in M23 and M31, along with a slight increase in bulk density as observed also by Zhang et al. (2019). Soil temperature, particularly freezing, is a factor that affects soil structure (Klöffel et al. 2024). For example, Abramyan et al. (2021) reported a decrease in porosity after freezing-thawing cycles. These cycles can reduce porosity, resulting in denser urban topsoil and mixed soil. Also Leuther and Schlüter (2021) claim that freezing-thawing cycles reduce pore size and pore connectivity, but only slightly affect macropore systems. Between M18 and M31, both BCs showed a slight decrease in total porosity when the biofilter froze. Macroporosity was minimally affected, with a slight decrease observed in BC1 and a slight increase in BC2 between M18 and M31, which is consistent with the findings of the previous study. Mohanty et al. (2014) proposed that ice freezing may create additional preferential paths flow. Based on Fig. 6, a decrease in connection probability was only observed in BC1 between M18 and M23. Mohanty et al. (2014) hypothesized that ice freezing could create additional preferential flow. These statements refer to the topsoil layer up to a depth of 10 cm. The biofilter in BCs was frozen only once during the observation period, at the beginning of 2019. At a depth of 12–13 cm, the temperature remained below 0 °C.

5 Conclusions

Early development of biofilter soil structure was evaluated on samples collected within 31 months after the establishment of two experimental bioretention cells with different water regimes that caused also differences in plants growth, especially in 2020, when BC2 was not anymore flooded by the ponding experiments. X-ray computed microtomography proved to be a suitable tool to analyze the characteristics of the soil pore space important to long-term functionality of the biofilter layer. In both bioretention cells studied, the expected soil consolidation occurred during first 12 months after BC establishment, characterized by a reduction in total porosity and macroporosity. Subsequently, consolidation continued in the BC with wetter water regime for another six months before macroporosity started to recover, while total porosity had already stabilized. The development of both, total porosity and macroporosity in the drier BC showed higher variability in between samples. Other parameters, namely the critical pore diameter and the normalized Euler number had also higher variability in drier BC than in wetter BC. The field capacity of wetter biofilter initially increased to eventually return to the original level after 31 months of BC operation. Overall, a decrease in field capacity was detected in the drier BC. A stronger correlation between macroporosity and the connection probability was observed in the case of the biofilter under the wetter water regime. It was stronger for the wetter water regime. The results suggest that the soil structure development was more uniform in the BC with wetter water regime than in the drier biofilter. Further studies should focus on tracing of origins of observed structural changes, namely the role of particles trapping in porosity reduction and role of soil fauna in total porosity and macroporosity recovery.

Supplementary Information The online version contains supplementary material available at https://doi.org/10.1007/s11368-024-03828-4.

Funding Open access publishing supported by the National Technical Library in Prague. This work has been supported by the Czech Science Foundation under Grant no. 22-25673S. Additionally, financial support was provided by the Grant Agency of the Czech Technical University in Prague, under the reference SGS23/154/OHK1/3T/11. The samples imaging at the Czech University of Life Sciences was supported by the NutRisk project with the identification number CZ.02.1.01/0.0/0.0/16_019/0000845.

Declarations

Conflict of interest The authors declare no competing interests.

Open Access This article is licensed under a Creative Commons Attribution 4.0 International License, which permits use, sharing, adaptation, distribution and reproduction in any medium or format, as long as you give appropriate credit to the original author(s) and the source, provide a link to the Creative Commons licence, and indicate if changes were made. The images or other third party material in this article are included in the article's Creative Commons licence, unless indicated otherwise in a credit line to the material. If material is not included in the article's Creative Commons licence and your intended use is not permitted by statutory regulation or exceeds the permitted use, you will need to obtain permission directly from the copyright holder. To view a copy of this licence, visit http://creativecommons.org/licenses/by/4.0/.

References

Abramoff M, Magalhães P, Ram SJ (2004) Image processing with ImageJ. Biophotonics Int 11:36–42

Abramyan AI, Ezhelev ZS, Umarova AB et al (2021) Effects of freezing-thawing cycles on porosity and geometric configuration of an artificial soils in laboratory modeling. IOP Conf Ser Earth Environ Sci 862:012037. https://doi.org/10.1088/1755-1315/862/1/012037

Archer NAL, Quinton JN, Hess TM (2002) Below-ground relationships of soil texture, roots and hydraulic conductivity in two-phase mosaic vegetation in South-east Spain. J Arid Environ 52:535–553. https://doi.org/10.1006/jare.2002.1011

Aydemir S, Keskin S, Drees LR (2004) Quantification of soil features using digital image processing (DIP) techniques. Geoderma 119:1–8. https://doi.org/10.1016/S0016-7061(03)00218-0

Badin A-L, Méderel G, Béchet B et al (2009) Study of the aggregation of the surface layer of Technosols from stormwater infiltration basins using grain size analyses with laser diffractometry. Geoderma 153:163–171. https://doi.org/10.1016/j.geoderma.2009.07.022

Baveye PC, Laba M, Otten W et al (2010) Observer-dependent variability of the thresholding step in the quantitative analysis of soil images and X-ray microtomography data. Geoderma 157:51–63. https://doi.org/10.1016/j.geoderma.2010.03.015

Bodner G, Leitner D, Kaul H-P (2014) Coarse and fine root plants affect pore size distributions differently. Plant Soil 380:133–151. https://doi.org/10.1007/s11104-014-2079-8

Chen X (2018) Earthworm positively influences large macropores under extreme drought conditions and conservation tillage in a Chinese Mollisol. Appl Ecol Environ Res 16:663–675. https://doi.org/10.15666/aeer/1601_663675

Cislerova M, Jirka SJ, Vogel T (1988) Changes of steady state infiltration rate in recurrent ponded infiltration experiments. J Hydrol 104:1–16. https://doi.org/10.1016/0022-1694(88)90154-0

Cnudde V, Boone MN (2013) High-resolution X-ray computed tomography in geosciences: A review of the current technology and applications. Earth-Sci Rev 123:1–17. https://doi.org/10.1016/j.earscirev.2013.04.003

Coustumer S, Fletcher T, Deletic A et al (2009) Hydraulic performance of biofilter systems for stormwater management: Influences of design and operation. J Hydrol 376:16–23. https://doi.org/10.1016/j.jhydrol.2009.07.012

Davis A (2008) Field performance of bioretention: Hydrology impacts. J Hydrol Eng. https://doi.org/10.1061/(ASCE)1084-0699(2008)13:2(90)

Deeb CM, Grimaldi M, Lerch T et al (2016) Influence of organic matter content on hydro-structural properties of constructed Technosols. Pedosphere 26:486–498. https://doi.org/10.1016/S1002-0160(15)60059-5

Deeb CM, Groffman P, Blouin M et al (2020) Using constructed soils for green infrastructure - challenges and limitations. SOIL 6:413–434. https://doi.org/10.5194/soil-6-413-2020

Dexter AR, Radke JK, Hewitt JS (1983) Structure of a tilled soil as influenced by tillage, wheat cropping, and rainfall. Soil Sci Soc Am J 47:570–575. https://doi.org/10.2136/sssaj1983.03615995004700030035x

Dietz ME (2007) Low impact development practices: A review of current research and recommendations for future directions. Water Air Soil Pollut 186:351–363. https://doi.org/10.1007/s11270-007-9484-z

Dietz ME, Clausen JC (2005) A field evaluation of rain garden flow and pollutant treatment. Water Air Soil Pollut 167:123–138. https://doi.org/10.1007/s11270-005-8266-8

Dohnal M, Jelinkova V, Snehota M et al (2013) Tree-Dimensional Numerical Analysis of Water Flow Affected by Entrapped Air: Application of Noninvasive Imaging Techniques. Vadose Zone J 12. https://doi.org/10.2136/vzj2012.0078

Emerson CH, Traver RG (2008) Multiyear and seasonal variation of infiltration from storm-water best management practices. J Irrig Drain Eng 134:598–605. https://doi.org/10.1061/(asce)0733-9437(2008)134:5(598)

Gerke H, Kuchenbuch R (2007) Root effects on soil water and hydraulic properties. Biologia (bratisl) 62:557–561. https://doi.org/10.2478/s11756-007-0110-8

Grevers MC, Jong ED, St. Arnaud RJ (1989) The characterization of soil macroporosity with ct scanning. Can J Soil Sci 69:629–637. https://doi.org/10.4141/cjss89-062

Hatt BE, Fletcher TD, Deletic A (2009) Hydrologic and pollutant removal performance of stormwater biofiltration systems at the field scale. J Hydrol 365:310–321. https://doi.org/10.1016/j.jhydrol.2008.12.001

Heckova P, Bareš V, Stránský D, Sněhota M (2022) Performance of experimental bioretention cells during the first year of operation. J Hydrol Hydromech 70:42–61. https://doi.org/10.2478/johh-2021-0038

Helliwell J, Sturrock C, Grayling K et al (2013) Applications of X-ray computed tomography for examining biophysical interactions and structural development in soil systems: A review. Eur J Soil Sci 64:n/a-n/a. https://doi.org/10.1111/ejss.12028

Jangorzo NS, Watteau F, Schwartz C (2013) Evolution of the pore structure of constructed Technosols during early pedogenesis quantified by image analysis. Geoderma 207:180–192. https://doi.org/10.1016/j.geoderma.2013.05.016

Jarvis N, Larsbo M, Koestel J (2017) Connectivity and percolation of structural pore networks in a cultivated silt loam soil quantified by X-ray tomography. Geoderma 287:71–79. https://doi.org/10.1016/j.geoderma.2016.06.026

Jelinkova V, Dohnal M, Sacha J (2016) Thermal and water regime studied in a thin soil layer of green roof systems at early stage of pedogenesis. J Soils Sediments 16. https://doi.org/10.1007/s11368-016-1457-7

Jenkins JKG, Wadzuk BM, Welker AL (2010) Fines accumulation and distribution in a storm-water rain garden nine years postconstruction. J Irrig Drain Eng 136:862–869. https://doi.org/10.1061/(asce)ir.1943-4774.0000264

Kaestner AP, Trtik P, Zarebanadkouki M et al (2016) Recent developments in neutron imaging with applications for porous media research. Solid Earth 7:1281–1292. https://doi.org/10.5194/se-7-1281-2016

Keller T, Colombi T, Ruiz S et al (2017) Long-Term Soil Structure Observatory for Monitoring Post-Compaction Evolution of Soil Structure. Vadose Zone J. https://doi.org/10.2136/vzj2016.11.0118

Klöffel T, Larsbo M, Jarvis N, Barron J (2024) Freeze-thaw effects on pore space and hydraulic properties of compacted soil and potential consequences with climate change. Soil Tillage Res 239:106041. https://doi.org/10.1016/j.still.2024.106041

Koestel J, Schlüter S (2019) Quantification of the structure evolution in a garden soil over the course of two years. Geoderma 338:597–609. https://doi.org/10.1016/j.geoderma.2018.12.030

Koestel J, Larsbo M, Jarvis N (2020) Scale and REV analyses for porosity and pore connectivity measures in undisturbed soil. Geoderma 366:114206. https://doi.org/10.1016/j.geoderma.2020.114206

Koestel J (2018) SoilJ: An ImageJ plugin for the semiautomatic processing of three-dimensional x-ray images of soils. Vadose Zone J. https://doi.org/10.2136/vzj2017.03.0062

Legland D, Arganda-Carreras I, Andrey P (2016) MorphoLibJ: Integrated library and plugins for mathematical morphology with

ImageJ. Bioinformatics 32:3532–3534. https://doi.org/10.1093/bioinformatics/btw413
Leuther F, Schlüter S (2021) Impact of freeze-thaw cycles on soil structure and soil hydraulic properties. SOIL 7:179–191. https://doi.org/10.5194/soil-7-179-2021
Liu H, Liu Z, Morató J et al (2022) Evaluation of substrate clogging in a full-scale horizontal subsurface flow treatment wetland using electrical resistivity tomography with an optimized electrode configuration. Sci Total Environ 824:153981. https://doi.org/10.1016/j.scitotenv.2022.153981
Malek K, Malek K, Khanmohammadi F (2021) Response of soil thermal conductivity to various soil properties. Int Commun Heat Mass Transf 127:105516. https://doi.org/10.1016/j.icheatmasstransfer.2021.105516
Messing I, Jarvis NJ (1990) Seasonal variation in field-saturated hydraulic conductivity in two swelling clay soils in Sweden. J Soil Sci 41:229–237. https://doi.org/10.1111/j.1365-2389.1990.tb00059.x
Mesticou Z, Kacem M, Dubujet P (2016) Coupling effects of flow velocity and ionic strength on the clogging of a saturated porous medium. Transp Porous Media. https://doi.org/10.1007/s11242-016-0644-8
Mohanty SK, Saiers JE, Ryan JN (2014) Colloid-facilitated mobilization of metals by freeze-thaw cycles. Environ Sci Technol 48:977–984. https://doi.org/10.1021/es403698u
Moller I, De Fine LH, Harholt J et al (2011) The dynamics of plant cell-wall polysaccharide decomposition in leaf-cutting ant fungus gardens. PLoS ONE 6:e17506. https://doi.org/10.1371/journal.pone.0017506
Muerdter C, Wong C, LeFevre G (2018) Emerging investigator series: The role of vegetation in bioretention for stormwater treatment in the built environment: Pollutant removal, hydrologic function, and ancillary benefits. Environ Sci Water Res Technol. https://doi.org/10.1039/C7EW00511C
Pagliai M, Vignozzi N, Pellegrini S (2004) Soil structure and the effect of management practices. Soil Tillage Res 79:131–143. https://doi.org/10.1016/j.still.2004.07.002
Paus KH, Muthanna TM, Braskerud BC (2016) The hydrological performance of bioretention cells in regions with cold climates: seasonal variation and implications for design. Hydrol Res 47:291–304. https://doi.org/10.2166/nh.2015.084
Reginato R, Bavel C (1962) Pressure cell for soil cores1. Soil Sci Soc Am J. https://doi.org/10.2136/sssaj1962.03615995002600010001x
Renard P, Allard D (2013) Connectivity metrics for subsurface flow and transport. Adv Water Resour 51:168–196. https://doi.org/10.1016/j.advwatres.2011.12.001
Rippner D, Raja P, Earles J et al (2022) A workflow for segmenting soil and plant X-ray computed tomography images with deep learning in Google's Colaboratory. Front Plant Sci. https://doi.org/10.3389/fpls.2022.893140
Sandin M, Koestel J, Jarvis N, Larsbo M (2017) Post-tillage evolution of structural pore space and saturated and near-saturated hydraulic conductivity in a clay loam soil. Soil Tillage Res 165:161–168. https://doi.org/10.1016/j.still.2016.08.004
Scalenghe R, Ferraris S (2009) The first forty years of a Technosol. Pedosphere 19:40–52. https://doi.org/10.1016/s1002-0160(08)60082-x
Schaap M, Leij F, Van Genuchten M (2001) ROSETTA: A computer program for estimating soil hydraulic parameters with hierarchical pedotransfer functions. J Hydrol 251:163–176. https://doi.org/10.1016/S0022-1694(01)00466-8
Schindelin J, Arganda-Carreras I, Frise E et al (2012) Fiji: An open-source platform for biological-image analysis. Nat Methods 9:676–682. https://doi.org/10.1038/nmeth.2019
Schlüter S, Großmann C, Diel J et al (2018) Long-term effects of conventional and reduced tillage on soil structure, soil ecological and soil hydraulic properties. Geoderma 332:10–19. https://doi.org/10.1016/j.geoderma.2018.07.001
Schlüter S, Sammartino S, Koestel J (2020) Exploring the relationship between soil structure and soil functions via pore-scale imaging. Geoderma 370:114370. https://doi.org/10.1016/j.geoderma.2020.114370
Schneider CA, Rasband WS, Eliceiri KW (2012) NIH image to ImageJ: 25 years of image analysis. Nat Methods 9:671–675. https://doi.org/10.1038/nmeth.2089
Séré G, Schwartz C, Ouvrard S et al (2010) Early pedogenic evolution of constructed Technosols. J Soils Sediments 10:1246–1254. https://doi.org/10.1007/s11368-010-0206-6
Sere G, Ouvrard S, Magnenet V et al (2012) Predictability of the evolution of the soil structure using water flow modeling for a constructed Technosol. Vadose Zone J 11:13. https://doi.org/10.2136/vzj2011.0069
Soto Gómez D, Pérez-Rodríguez P, Vázquez L et al (2018) A new method to trace colloid transport pathways in macroporous soils using X-ray computed tomography and fluorescence macrophotography. Eur J Soil Sci. https://doi.org/10.1111/ejss.12783
Tan X, Chen W, Tian H, Cao J (2011) Water flow and heat transport including ice/water phase change in porous media: Numerical simulation and application. Cold Reg Sci Technol 68:74–84. https://doi.org/10.1016/j.coldregions.2011.04.004
Vanderborght J, Gähwiller P, Flühler H (2002) Identification of transport processes in soil cores using fluorescent tracers. Soil Sci Soc Am J. https://doi.org/10.2136/sssaj2002.0774
Wang N, Zhang T (2024) Soil pore structure and its research methods: A review. Soil Water Res. https://doi.org/10.17221/64/2023-SWR
Watteau F, Jangorzo NS, Schwartz C (2019) A micromorphological analysis for quantifying structure descriptors in a young constructed Technosol. Bol Soc Geológica Mex 71:11–20. https://doi.org/10.18268/BSGM2019v71n1a2
XLSTAT Lumivero [software] (2024). Retrieved from https://lumivero.com/products/xlstat/
Yuan J, Dunnett N (2018) Plant selection for rain gardens: Response to simulated cyclical flooding of 15 perennial species. Urban for Urban Green 35:57–65. https://doi.org/10.1016/j.ufug.2018.08.005
Zanin G, Bettella F, Bortolini L (2018) Hydrological and plant performance of green roofs in the climate context of the Veneto Plain (north-eastern Italy): Preliminary results. Acta Hortic. https://doi.org/10.17660/ActaHortic.2018.1215.17
Zhang Q, Shao M, Jia X, Wei X (2019) Changes in soil physical and chemical properties after short drought stress in semi-humid forests. Geoderma 338:170–177. https://doi.org/10.1016/j.geoderma.2018.11.051
Zhou J, Xiong J, Xie X, Liu Y (2023) Clogging mechanism of bioretention cell with fine-grained soil medium. J Water Process Eng 53:103630. https://doi.org/10.1016/j.jwpe.2023.103630
Zhou H, Whalley R, Hawkesford M et al (2020) The interaction between wheat roots and soil pores in structured field soil. J Exp Bot. https://doi.org/10.1093/jxb/eraa475

Publisher's Note Springer Nature remains neutral with regard to jurisdictional claims in published maps and institutional affiliations.